Materials Today Chemistry 15 (2020) 100226

Contents lists available at ScienceDirect

Materials Today Chemistry

journal homepage: www.journals.elsevier.com/materials-today-chemistry/

Improved chemical water oxidation with Zn in the tetrahedral site of spinel-type $ZnCo_2O_4$ nanostructure

B. Chakraborty [a], A. Indra [b], P.V. Menezes [c], M. Driess [a, **], P.W. Menezes [a, *]

[a] Department of Chemistry, Metalorganics and Inorganic Materials, Technische Universität Berlin, Strasse des 17. Juni 135, Sekr. C2, 10623 Berlin, Germany
[b] Department of Chemistry, Indian Institute of Technology (BHU), Varanasi, Uttar Pradesh 221005, India
[c] Institut für Elektrochemie, Universität Ulm, Albert-Einstein-Allee 47, D-89 081 Ulm, Germany

ARTICLE INFO

Article history:
Received 16 October 2019
Received in revised form
6 November 2019
Accepted 7 November 2019
Available online xxx

Keywords:
$ZnCo_2O_4$ nanochains
Spinel-type structure
Tetrahedral versus octahedral site
Chemical water-oxidation
Sustainable catalyst

ABSTRACT

Spinel oxides with the composition of $A^{II}B^{III}{}_2O_4$ (A and B are metal ions) represent an important class of anode material for water splitting to replace the currently used noble-metal catalysts. Although spinel electrocatalysts have widely been investigated for electrochemical water oxidation, the role of octahedral and tetrahedral sites influencing catalytic performance has been a topic of discussion for a long time and still under debate. Lately, this issue has been addressed by substituting redox-inert cation to the tetrahedral sites of cobalt spinels and comparing the electrochemical activity between them. However, rapid surface structural transformation of the catalysts under operating electrochemical conditions makes it difficult to infer the exact contribution of tetrahedral and octahedral sites for water oxidation. Herein, for the first time, we utilize the oxidant-driven water oxidation approach to reveal the responsible active sites using two spinel-type nanostructures, $Zn^{II}Co_2^{III}O_4$ and $Co^{II}Co_2^{III}O_4$ (Co_3O_4), synthesized by using a single-source precursor approach. Strikingly, a superior O_2 production rate (0.98 $mmol_{O2}$ mol_{Co}^{-1} s^{-1}) following first-order reaction kinetics was achieved for $ZnCo_2O_4$ in the presence of Ce^{IV} as sacrificial electron acceptor compared to Co_3O_4 spinel (0.29 $mmol_{O2}$ mol_{Co}^{-1} s^{-1}). The structural and morphological stability of the $ZnCo_2O_4$ and Co_3O_4 post water oxidation catalysis confirms that the catalytic activity is strictly controlled by the geometry and electronic structure of the active site of the spinel structure. The higher performance of $ZnCo_2O_4$ over Co_3O_4 further indicates that the presence of Co^{II} is not essential for catalytic water oxidation. The presence of redox inert Zn^{II} at the tetrahedral site of $ZnCo_2O_4$ can facilitate the stabilization of a high-valent Co^{IV} intermediate via oxidation of Co^{III} (situated at the octahedral site), and this intermediate can be regarded as the active species for water oxidation catalyst along with structural defects caused by surface Zn leaching.

1. Introduction

Oxidation of water to oxygen is one of the important reactions occuring during photosynthesis, a natural photochemical process to store solar energy to chemical energy [1,2]. However, sluggish kinetics of this thermodynamically uphill four-electron oxidation reaction remains a potential bottleneck [3]. Development of an active catalyst, which could overcome this potential problem, is indeed a perdurable challenge, and over the past few decades [4], a number of catalysts have been designed to accelerate the oxygen evolution reaction (OER) under a mild reaction condition with favorable kinetics [5–8]. Although the best-known catalyst for OER is still based on the precious-metal catalysts (IrO_2 and RuO_2), scarcity, prohibitive cost, and declining activity greatly restrict their use for large-scale applications [9,10]. In this regard, tremendous efforts have been made to develop efficient and durable OER catalysts based on the earth-abundant non-precious metals [11–21]. Among them, transition metal oxides with enhanced conductivity and highly accessible active sites have received significant attention and demonstrated as potential OER catalysts to replace currently used state-of-the-art catalysts [14,22–31].

Spinels are the most abundant natural mineral, all of which are oxides with the general formula $A^{II}B^{III}{}_2O_4$, where metal A occupies the centers of tetrahedrally (T_d) coordinated positions and metal B is in the octahedral (O_h) environment. Depending on the metal

* Corresponding author.
** Corresponding author.
E-mail addresses: matthias.driess@tu-berlin.de (M. Driess), prashanth.menezes@mailbox.tu-berlin.de (P.W. Menezes).

https://doi.org/10.1016/j.mtchem.2019.100226
2468-5194/

cations, huge diversity in the structure-function of spinels can be achieved by altering suitable $A^{II}{}_{Td}$ site and $B^{III}{}_{Oh}$ sites [32]. Over the years, numerous spinels with varying T_d and O_h sites have also been investigated for electrochemical OER, and among them, cobalt oxide (Co_3O_4 is the $Co^{II}Co^{III}_2O_4$ spinel) has received great interest and has been widely used as OER electrocatalyst displaying promising activities and stabilities in alkaline and neutral media [33–37]. In the Co_3O_4 spinel structure, two types of cobalt centers are present, in which the geometry and oxidation of the cobalt center are completely different. The divalent cobalt metal (Co^{II}) is located at the T_d site, whereas the Co^{III} preferably situated at the O_h site, and the population of each site strictly controls the reactivity [38–43]. The extent of orbital overlap of the bridging oxygen toward both metal sites is equally a governing factor to determine the reactivity. Previous studies have shown that a major charge donation to $Co^{III}{}_{Oh}$ by oxygen results in higher orbital overlap resulting O_h site most active for OER [44–46]. This correlation was further established by applying two spinels, Co_3O_4 and $ZnCo_2O_4$, for alkaline OER, where strikingly superior activity for the latter was attained, signifying the prominence of O_h sites as well as vacancy-induced surface by Zn leaching [41]. Conversely, using three homologous spinels, Co_3O_4, $ZnCo_2O_4$, and $CoAl_2O_4$, designed by the careful choice of divalent and trivalent metal ions, the role of tetrahedral $Co^{II}{}_{Td}$ site in the formation of *in situ* cobalt oxyhydroxide (CoOOH) to catalyze the water oxidation has also been reported [47,48]. As these catalysts are converted to active phase CoOOH by anodic oxidation, the role of the cations in O_h and T_d sites during water oxidation cannot be assigned unambiguously [49]. In this respect, oxidant-driven water oxidation can be more useful to understand the effect of T_d and O_h occupancy of the metal ions in O–O bond formation. Although, the electrocatalytic OER with cobalt-based spinels being studied for the past few years and the partial mechanistic detail has been uncovered [50], the potential of this class of material and the influence of O_h and T_d sites in chemical oxidation of water have not been explored yet.

Herein, two spinel-type $ZnCo_2O_4$ and Co_3O_4 nanostructures have been applied for the first time as active catalysts for chemical oxidation of water using ceric ammonium nitrate (CAN) as the sacrificial electron acceptor. The rate of oxygen production of $ZnCo_2O_4$ has been found to be superior in comparison to Co_3O_4 and other two different-type nanostructures, Co_3O_4@ZnO and ZnO. Highest O_2 production rate with the $ZnCo_2O_4$ spinel nanostructure emphasizes the structural role of the redox-active $Co^{III}{}_{Oh}$ site and the redox inactive $Zn^{II}{}_{Td}$ site in $ZnCo_2O_4$. Post-catalytic analyses performed herein ensure the structural rigidity of the catalysts under oxidative reaction conditions.

2. Results and discussion

$ZnCo_2O_4$ and Co_3O_4 nanomaterials were prepared from their respective hydroxide-carbonate precursors, following a previously reported annealing method [41,42]. Powder X-ray diffraction (PXRD) of the materials confirmed the formation of phase pure $ZnCo_2O_4$ (JCPDS 23-1390) and Co_3O_4 (JCPDS 42-1467) (Fig. S1a,b). As observed from the intense reflections of the diffraction patterns (PXRD), both $ZnCo_2O_4$ and Co_3O_4 display high crystallinity and the crystals belong to the cubic system with space group *Fd*3*m* (Nr. 227) with a cell length of 8.08 ± 2 Å. However, the close packing of the atoms inside the lattice structure indicates that metal (M) atoms possess two different coordination geometries, octahedral (MO_6) and tetrahedral (MO_4), surrounded by the oxygen atoms confirming the spinel structure (Fig. 1a–b) [32,38,40]. Crystal structure analysis affirmed that T_d sites are preferably occupied by divalent metal ions, and the trivalent metal ions are located at the O_h sites [44]. In such a situation, Zn^{II} and Co^{II} in $ZnCo_2O_4$ and Co_3O_4, respectively, are located at the T_d geometry (Fig. 1b), while O_h sites in both oxides are occupied by Co^{III} ion (Fig. 1b). In this particular arrangement of atoms inside the spinel lattice, each oxygen atom is coordinated to four nearest neighboring cations, of which one is linked to a T_d site and the rest three are in O_h environment [44]. However, the electronic structure of the spinel, for instance, splitting of the d-orbitals of the metal ions in these two different sites, is predominantly governed by the competitive bonding participation of the metal's 3d orbitals with oxygen's orbital [51].

The elemental composition of the as-prepared $ZnCo_2O_4$ and Co_3O_4 materials was confirmed from the inductively coupled plasma atomic emission spectroscopy (ICP-AES) and that was found to be in accordance with the derived chemical formulae predicted from the PXRD (Table S1). To elucidate the morphology and structure of both $CoZn_2O_4$ and Co_3O_4 spinels, extensive microscopic analyses were performed. Scanning electron microscopic (SEM) images of the as-prepared $ZnCo_2O_4$ exhibited a nanochain morphology (Fig. 2a) with the aggregation of the chain builds a near-spherical coral-shaped colony (Fig. S2). This nanochain morphology was also evidenced by the transmission electron microscopy (TEM), which displayed, on average, nanochains of 0.5 μm long and diameter ca. 50 nm (Fig. S3). High-resolution (HR) TEM images of $ZnCo_2O_4$ suggested that each chain was built up by assembling several 5–10 nm nearly spherical nanoparticles (Fig. 2b). The HR-TEM image also clearly indicated the high crystallinity of the individual particles, and the phase purity was established from the atomic fringes that matched perfectly with the (400) planes at a d-spacing of 2.06 Å. Furthermore, the well-defined reflections from the selected area electron diffraction (SAED) pattern exerted from the particles of TEM images confirms the purity and crystallinity of $ZnCo_2O_4$ (inset Fig. 2c). The elemental mapping from energy-dispersive X-ray spectroscopic (EDX) analysis was performed while accumulating the SEM images (Fig. S4), which indeed substantiated the homogeneous distribution of Zn, Co, and O in the $ZnCo_2O_4$ nanoparticle (Fig. 2d–g) (Table S1). Unlike $ZnCo_2O_4$ nanochains, the SEM image of Co_3O_4 nanoparticles displayed a spherical morphology (Fig. S5a), which was also evident from the TEM image. Furthermore, the TEM image suggested the distribution of the particle size ranging from 40 to 80 nm (Fig. S5b), while the HR-TEM image revealed the atomic fringes of Bragg's planes (111) and (400) with comparable d-spacing values as reported earlier (Fig. S5c). Additionally, multiple well-resolved ring patterns in the SAED confirm the purity and high crystallinity of Co_3O_4 nanospheres (Fig. S5d). The presence of Co and the elemental composition of the Co_3O_4 were confirmed by EDX analysis (Fig. S6).

The chemical state of both $ZnCo_2O_4$ and Co_3O_4 was examined by using X-ray photoelectron spectroscopy (XPS). In general, Co^{II} and Co^{III} have almost similar 2p binding energies. However, they can still be distinguished by the Co $2p_{3/2}$–$2p_{1/2}$ spin-orbit-level energy spacing, which is 16.0 eV for high-spin Co^{II} and 15.0 eV for low-spin Co^{III} [41]. In the case of $ZnCo_2O_4$, the Co 2p spectrum consists of two spin-orbit components, Co $2p_{3/2}$ and Co $2p_{1/2}$, at the binding energy of 779.7 eV and 794.7 eV, which is close to 15 eV and in accordance with the values of Co^{III} (Fig. 2h and Fig. S7) [16–18]. However, in the case of Co_3O_4, the binding energy of Co $2p_{3/2}$ was situated at 780.2 eV, while Co $2p_{1/2}$ was centered at 795.8 eV, with a total difference of 15.6 eV and is consistent with the values of Co^{II}/Co^{III} (Figs. S7 and S9) [15,16]. Similarly, the Zn 2p spectra of $ZnCo_2O_4$ exhibited two peaks at 1022.6 and 1044.9 eV associated with Zn $2p_{3/2}$ and Zn $2p_{1/2}$, respectively, confirming the presence of Zn^{II} (Fig. 2i) [41]. The O 1s spectra in both $ZnCo_2O_4$ and Co_3O_4 can be deconvoluted into three peaks at around 529.7 (O1), 532 (O2), and 533.7 eV (O3), which could be ascribed to oxide (O^{2-}) present in different coordination geometries, some surface hydroxide, as well as adsorbed water (Figs. S8 and S9). The binding energies attained

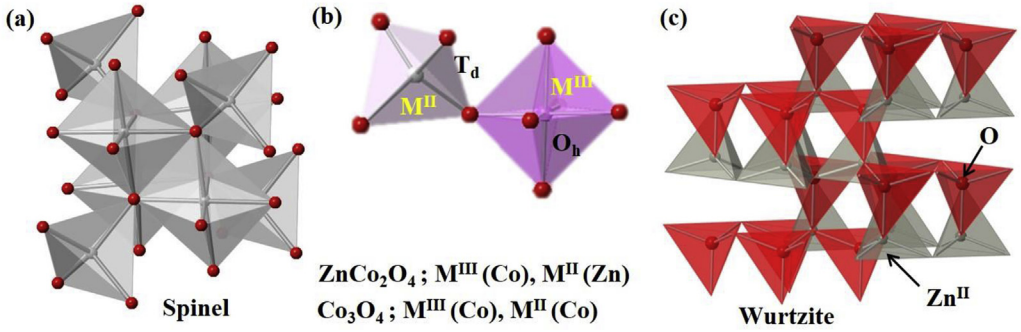

Fig. 1. Polyhedral (with a ball and stick as the backbone) representation of (a) the unit cell of the spinel Co_3O_4 and $ZnCo_2O_4$ nanostructure crystallized in the cubic system with space group *Fd*3*m* (Nr. 227) exhibiting (b) two individual coordination sites of metals; O_h (purple) and T_d (gray). A spinel is represented with the general formula $A^{II}B^{III}{}_2O_4$ and, Zn^{II} in $ZnCo_2O_4$, as well as Co^{II} in Co_3O_4, occupied the T_d (gray) sites. However, the O_h (purple) sites of both structures are acquired by Co^{III}. (c) The polyhedral presentation of wurtzite-type ZnO lattice with space group $P6_3mc$ (No. 186) where both Zn^{II} and oxygen are located at the T_d site. (For interpretation of the references to color in this figure legend, the reader is referred to the Web version of this article).

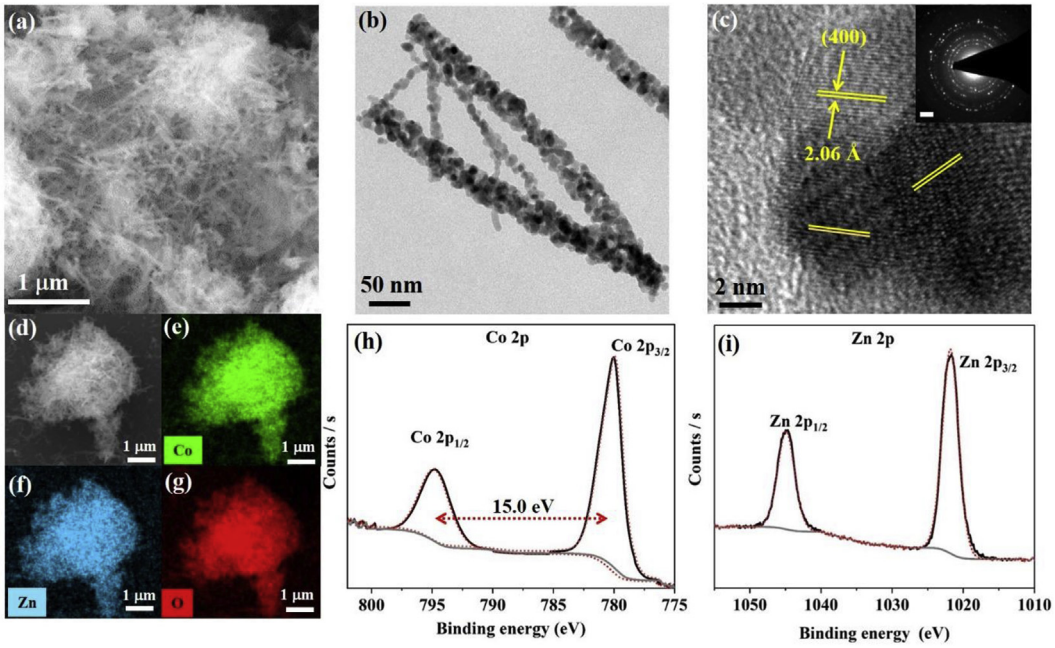

Fig. 2. (a) SEM image of multiple $ZnCo_2O_4$ nanochain assembly, (b) TEM image of $ZnCo_2O_4$ nanochains consisting of 5–10 nm individual nanoparticle, (c) HR-TEM image of the nanoparticle with atomic fringes for (400) planes (SAED pattern with well-defined diffraction rings are shown in the inset), (d–g) elemental mapping (EDX-SEM) of the nanochain assembly representing a homogeneous distribution of (e) Co, (f) Zn, and (g) O. High-resolution XPS spectra of (h) Co 2p and (i) Zn 2p.

in each case are in accordance with the values of spinel metal oxides reported in the literature [15–18], and the corresponding detailed deconvolution of XPS has been provided in Fig. 2h–i and Figs. S7–S9. Finally, the Brunauer–Emmett–Teller (BET) surface areas were also determined where a high surface area of 56.5 m^2/g was achieved for $ZnCo_2O_4$, whereas lower surface area (38 m^2/g) resulted in Co_3O_4 nanostructures, showing the introduction of Zn in the T_d structure of $ZnCo_2O_4$ markedly increased the overall surface area.

To have more clarity on the structural influencing the activity, a polycrystalline Co_3O_4@ZnO (precisely $Co_3O_4/(ZnO)_6$, Table S1) and nearly spherical ZnO nanocrystals were also synthesized following a similar reaction condition by varying the composition of the carbonate-hydroxide precursors [41,42]. Detailed structural analysis of Co_3O_4@ZnO revealed that Co_3O_4 nanocrystals were deeply embedded in ZnO (Figs. S1 and S10), while ZnO shows highly crystalline hexagonal wurtzite-type lattice with space group $P6_3mc$ (No. 186) where Zn^{II} is located at the tetrahedral site (Fig. 1c; Figs. S1, S11, S12) [52].

In recent reports, the spinels have been often considered as an excellent class of water oxidation electrocatalysts [19,37,41,42,44,46–48,50]. Here, for the first time, we elucidate the spinel-type nanocrystals as potential heterogeneous catalysts for chemical oxidation of water. Over the decades, ceric ammonium nitrate (CAN) has been used as a potent oxidizing agent in chemical water oxidation reaction with soluble molecular catalysts [53–55]. Detailed kinetic and mechanistic analyses suggest that Ce^{IV}, having a high redox potential (E^0 = 1.7 V versus the normal hydrogen electrode, NHE), is capable of promoting the active metal center of the catalyst to a high-valent oxidation state, which spontaneously oxidizes water and, as a consequence, Ce^{IV} is reduced to Ce^{III}. Therefore, the oxidant-driven OER experiments (see Experimental) were conducted with all as-synthesized catalysts in the deoxygenated aqueous solution of 0.5 M CAN. The addition of CAN

solution to the well-dispersed aqueous solution of the metal-oxide catalysts results in a spontaneous formation of O_2 bubbles, indicating oxidation of water under acidic conditions (pH = 1) (Scheme 1). As displayed in Fig. 3a, the dissolved oxygen concentration in the solution for all catalysts was monitored for 600 s and a maximum of 461 μmol L^{-1} of O_2 was produced for $ZnCo_2O_4$, which was the best value of oxygen recorded among all the investigated materials. The superiority of $ZnCo_2O_4$ over Co_3O_4 is also in line with the electrochemical OER results recently reported by us [41].

To understand the reaction kinetics of the chemical water oxidation, O_2 production was monitored with time for each catalyst. Under our experimental condition, in the aqueous (ca. 55 M H_2O) reaction mixture, CAN (0.5 M) was present as many folds excess in compared to the catalyst concentration (1 mg in 2 mL), which is necessary to overcome the kinetic barrier of the water oxidation reaction. Under the reaction condition, notably, time traces for O_2 production (for all the catalysts) followed first-order reaction kinetics, as depicted from the exponential and linear fits of the time traces (Fig. 3b and Figs. S13–S16). The calculated rate constant (k_{obs}) is 10.7×10^{-3} s^{-1} with $ZnCo_2O_4$, which is higher than that of Co_3O_4 (Table S2). Not only the rate constant for the chemical water-oxidation with $ZnCo_2O_4$ is the highest among this series of materials, but also the initial rate of the reaction calculated from a linear fitting of the first few seconds (the method of initial rates) exceeds the rate observed for all the metal-oxide catalysts used (Fig. 3c, Table S2). Furthermore, a maximum rate of 0.98 $mmol_{O2}$ mol_{Co}^{-1} s^{-1} was achieved for $ZnCo_2O_4$ (considering only Co atoms are active) followed by 0.29 and 0.08 mmol mol_{Co}^{-1} s^{-1} for Co_3O_4 and Co_3O_4@ZnO, respectively, whereas ZnO was barely functioning. The values displayed here are clearly higher than other known Co-Zn-based materials and comparable to benchmark transition-metal oxide-based catalysts [19,56–58]. To have a fair comparison, the evolved O_2 rate was normalized with respect to the BET-specific surface area where the superior catalytic activity of $ZnCo_2O_4$ was achieved over Co_3O_4 establishing the critical role of T_d and O_h sites within both materials (Fig. 3d).

Recent literature studies have revealed that the manganese oxide-based catalysts could be transformed (in ~10–15 min) into active amorphous MnO_x catalysts for effective water oxidation using CAN as an oxidizing agent [30,31,59]. However, under electrochemical reaction conditions, the spinel-type Co_3O_4 and $ZnCo_2O_4$ catalysts undergo spontaneous surface restructuring, forming a thin layer of active cobalt-oxide/(oxy)hydroxide, which has been regarded as the active structure for OER catalysis [41,42,47]. This led us to investigate the stability and active structure of spinel oxide catalysts after CAN treatment. When examined, an almost comparable PXRD pattern with no change in phase was attained for both $ZnCo_2O_4$ and Co_3O_4 catalyst after oxidant-driven water oxidation within the tested period (Fig. 4a). Similar to PXRD, the TEM and HR-TEM images also suggested unaltered morphology of $ZnCo_2O_4$ (Fig. 4b and c, Fig. S17), and SAED patterns (Fig. 4b inset) confirmed the preservation of its high crystallinity. The elemental composition of the used catalysts was further verified by EDX analyses (after CAN treatment), where the presence of all required elements, as well as the absence of Ce, was observed, which is also consistent with the as-prepared materials (Fig. S18). The ICP-AES analysis suggested a slight amount of Zn (ca. 10%) loss from the structure of $ZnCo_2O_4$ without Ce incorporation, as confirmed by EDX analysis. Gaussian fitting of the prominent Bragg's reflection at 2θ of 36.7° (for [311] plane) provided the full width at half maximum (FWHM) that indicated a minor peak broadening after catalysis, and this could be ascribed to structural defects arising from zinc loss (Fig. S19). Although, the Co_3O_4 nanostructure after catalytic water oxidation underwent minimal transformation (Fig. S20), the peak broadening in PXRD leading to significant change in the calculated FWHM at 2θ of 36.7° suggested the loss of Co^{II}_{Td} from Co_3O_4 and simultaneous redeposition (verified by ICP-AES) at the surface (Fig. S21), which is also evident from the change in particle shape and crystallite size, as analyzed by TEM (Figs. S21 and S22). Furthermore, XPS of both catalysts were (Figs. S23 and S24) conducted to compare the change in the oxidation state of Co at the surface of the catalyst to that of the as-synthesized catalysts. Interestingly, the Co 2p XPS of $ZnCo_2O_4$ did not display any change in its peak shape, the oxidation state, as well as Co $2p_{3/2}$–$2p_{1/2}$ spin-orbit level energy spacing, whereas a slight amount of the Zn^{II} was lost from the surface of $ZnCo_2O_4$ (Fig. 4d–e), suggesting a defected and disordered surface [41]. The remaining Zn^{II} of $ZnCo_2O_4$ conserves its oxidation state (Fig. S23). By deconvoluting Co 2p envelop and evaluating Co^{III} and Co^{II} areas of Co_3O_4, it was evident that a higher fraction of Co^{III} was present on the surface after water oxidation (Fig. S23, Table S3). Besides, O 1s XPS spectra of both catalysts displayed the presence of a higher fraction of −OH groups (Fig. 4f) and O^{2-} region, indicating that the surface of the material was hydroxylated (Figs. S23–S24). The results acquired here signifies the surface oxidation of the catalyst influenced by oxidizing agents. Both Co_3O_4@ZnO and ZnO were not stable in the acidic pH and subsequently underwent slow dissolution.

Structural and activity correlation from the previous electrochemical study with the regular Co_3O_4 spinel has revealed that the Co^{III}_{Oh} sites at the surface are the real active species for OER, whereas the Co^{II}_{Td} sites are catalytically inactive, and consequently, the same trend has been followed for the substituted cobalt oxides [60]. The similar conclusions have also been drawn from the detailed X-ray absorption analysis where the prominence of O_h sites has been demonstrated [60–62]. Very recently, a comprehensive electrochemical study followed by extended X-ray

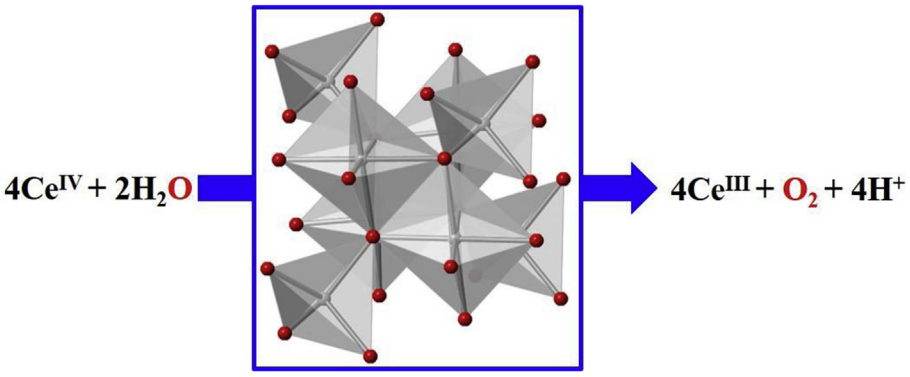

Scheme 1. Chemical oxidation of water using spinel-type nanomaterial catalysts in the presence of CAN as a sacrificial oxidant.

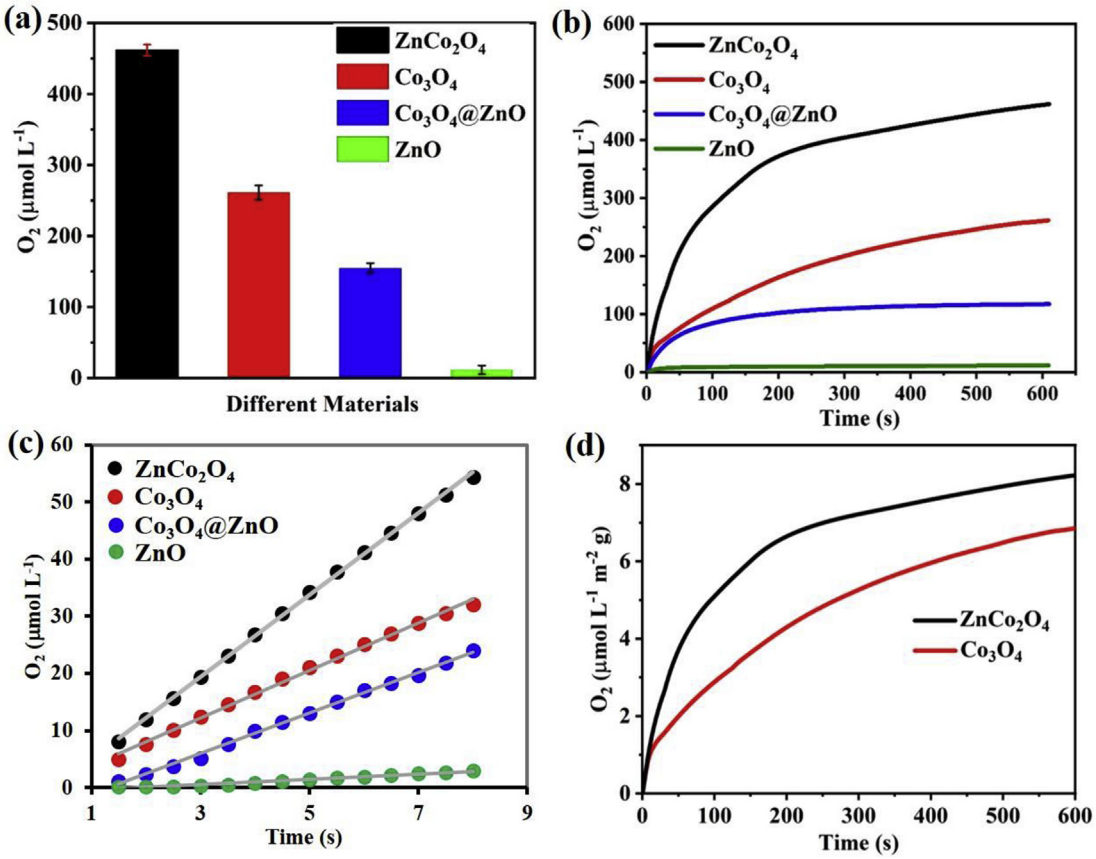

Fig. 3. Production of O_2 by chemical oxidation of water with nanomaterials ($ZnCo_2O_4$, Co_3O_4, Co_3O_4@ZnO, and ZnO) in the presence of CAN as oxidant; (a) comparison of the amount of dioxygen produced (after 10 min) with different nanomaterials used as catalysts, (b) profiles of O_2 production (in μmol L^{-1}) versus time with various catalysts, (c) calculation of initial rate of O_2 production (from the slope of the linear fitting of the plot of oxygen production per second), (d) oxygen concentrations normalized to the specific surface area measured from BET.

absorption fine structure (EXAFS) analysis with Co_3O_4 provided a new insight toward the structural correlation (active sites) with the OER activity where it was proposed that the Co^{II}_{Td} at the tetrahedral sites form an active CoOOH influencing the overall performance of water oxidation [47]. However, an in-depth theoretical calculation on the intrinsic OER activity of three spinels Co_3O_4, $ZnCo_2O_4$, and $CoAl_2O_4$ predicted the apparent orbital contribution of the bridging oxygen toward the O_h and T_d metal sites [48]. The calculation further established the crucial role of the bridging oxygen shared between the three Co^{III}_{Oh} and one Co^{II}_{Td} that strongly evidenced that the charge of the bridging oxygen more polarized toward Co^{III}_{Oh} instead of Co^{II}_{Td} making a strong Co–O interaction when acting as active sites for OER [44]. Recent reports on the cobalt-based materials have substantiated rapid oxidation of Co^{III}_{Oh} at the surface (under electrochemical reaction condition) to a putative Co^{IV} species, and the electrophilicity of the high-valent Co^{IV} facilitates O–O bond formation via a nucleophilic attack of water (Scheme 2) [63–65]. Strikingly, from the presented comparative study on oxidant-driven water oxidation, the higher activity of $ZnCo_2O_4$ over Co_3O_4 can be attributed to (i) the higher surface area of $ZnCo_2O_4$ that increases the accessible active sites, (ii) noncritical character of Co^{II}_{Td}, (iii) more significant amount of Co^{III}_{Oh} sites at the surface (iv) slight loss of the Zn^{II}_{Td} site surface to create surface structural defects, (v) remaining Zn^{II}_{Td} sites acting as Lewis acid to stabilize the high-valent Co^{IV} species to catalyze the reaction of water oxidation, which also consistent with the recent conclusions based on the electrochemical water oxidation [41].

3. Conclusion

In conclusion, the highly crystalline regular spinel-type $ZnCo_2O_4$ and Co_3O_4 nanomaterials have been synthesized by a straightforward annealing strategy using metal-hydroxide-carbonate precursors. The packing of the atoms in the crystal structure allows both materials to form a similar cubic-type lattice and a spinel structure occupying Co^{III} in the O_h sites, whereas Zn^{II} (in $ZnCo_2O_4$) and Co^{II} (in Co_3O_4) in T_d sites. Under oxidant-driven water oxidation conditions in CAN solution, a superior O_2 evolution activity was attained for $ZnCo_2O_4$ compared to Co_3O_4. By varying the conditions at the precursor level, Co_3O_4@ZnO and ZnO materials were also prepared as references exhibiting limited activity. Post-catalytic analysis of $ZnCo_2O_4$ reveals structural retention, except for a slight loss of Zn^{II} from the surface to introduce a highly active defect-spinel structure, exposing a higher amount of Co^{III} sites, while Co^{II}_{Td} of Co_3O_4 were also slightly oxidized. Based on our results, a tentative surface structure of $ZnCo_2O_4$ transpired where Co^{III}_{Oh} site acts as the active center and the Zn^{II}_{Td} site situated adjacent to the active site act as Lewis acid to stabilize the high-valent Co^{IV} species to catalyze the reaction of water oxidation, thus addressing the benefit of $ZnCo_2O_4$ over Co_3O_4. The study presented herein opens a new insight into material design, and particularly the T_d sites with different metal cations to expose more O_h sites that, in turn, could dramatically improve the chemical and photochemical water oxidation activity. Furthermore, elucidation of the nature of catalytically active center and the reaction mechanism using advanced

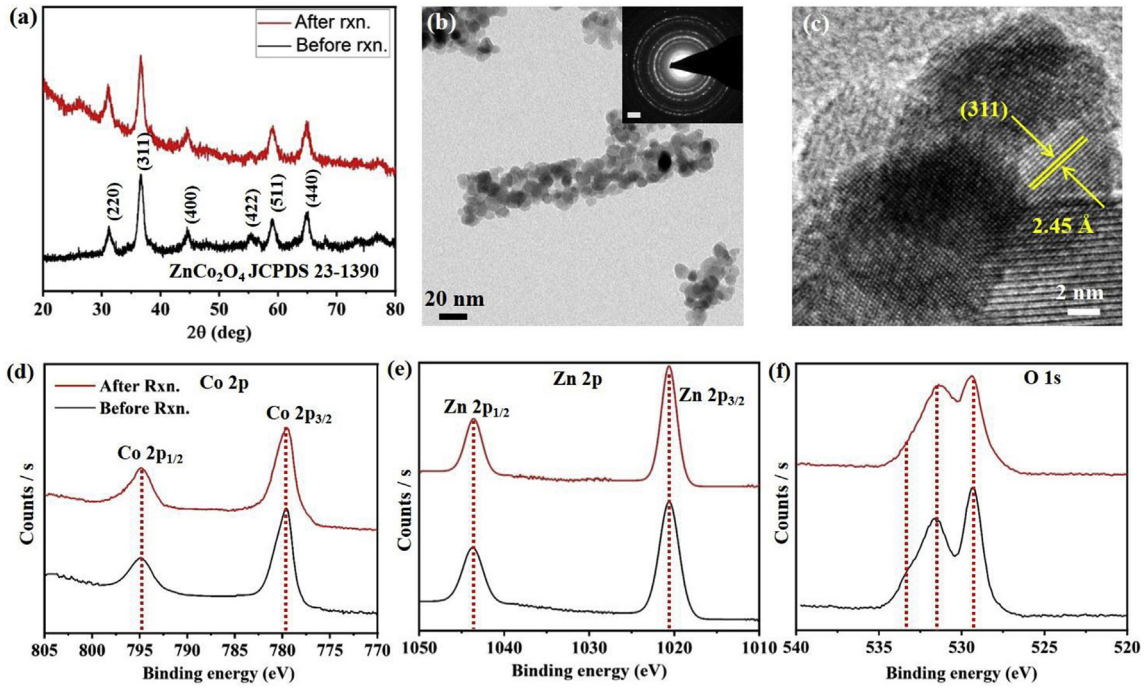

Fig. 4. Post-catalytic characterization of $ZnCo_2O_4$. (a) PXRD pattern of the $ZnCo_2O_4$ catalyst before reaction with CAN (black curve; with a correlation to the diffraction planes to the PDF pattern refereed in 23–1390) and after reaction with CAN (red curve), (b) TEM image of the nanochains consisting of several 5–10 nm nanoparticles (inset the SAED with strong diffraction rings for the crystalline $ZnCo_2O_4$ nanoparticles), (c) HR-TEM image depicting the atomic fringes of (311) planes with an inter-planar distance of 2.45 Å, (d–f) high-resolution XPS analysis of the Co 2p, Zn 2p and O 1s envelopes found for the $ZnCo_2O_4$ before (black curve) and after reaction CAN (red curve). (For interpretation of the references to color in this figure legend, the reader is referred to the Web version of this article.)

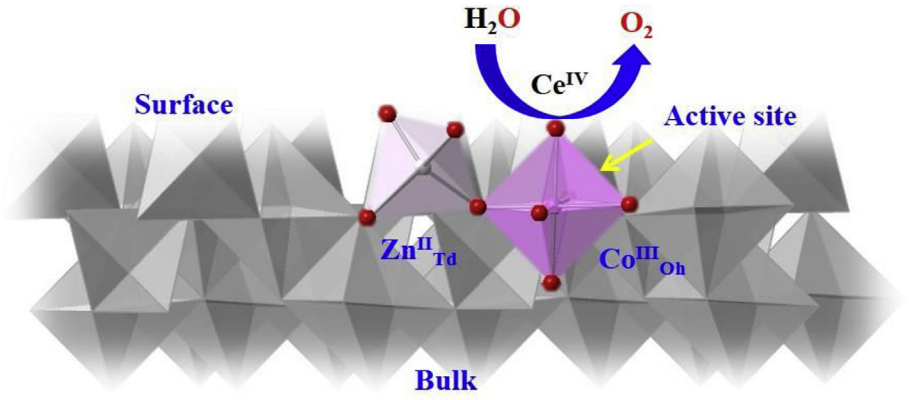

Scheme 2. Oxidation of water at the octahedral Co^{III} active site (purple translucent polyhedron with balls and stick) of $ZnCo_2O_4$ spinel-type nanocrystals, while the $Zn^{II}{}_{Td}$ site (light pink translucent polyhedron with red balls and stick) helps to stabilize the high-valent Co^{IV} intermediate species. The packing of the metal oxide layer at the surface is drawn from the cubic lattice of $ZnCo_2O_4$.

operando spectroscopic techniques will also be of particular interest for the future advancement of water oxidation.

4. Experimental section

Chemicals: All chemical reagents (analytical grade) were used as received without any further purification. Deionized water was used throughout the experiment.

Characterization: PXRD patterns were obtained on a Bruker AXS D8 advanced automatic diffractometer equipped with a position-sensitive detector (PSD) and curved germanium (111) primary monochromator using Cu Kα radiation (λ = 1.5418 Å). ICP-AES was carried out in a thermo jarrell ash trace scan analyzer. The samples were digested in aqua regia, and the average of three reproducible independent experiments has been presented. SEM was carried out on an LEO DSM 982 microscope integrated with EDX (EDAX, Apollo XPP). Data handling and analyses were achieved with the software package EDAX. TEM was accomplished on an FEI Tecnai G2 20 S-TWIN transmission electron microscope (FEI Company, Eindhoven, the Netherlands) equipped with a LaB_6 source at 200 kV acceleration voltage. Energy dispersive X-ray (EDX) analyses were achieved with an EDAX r-TEM SUTW detector (Si (Li) detector), and the images were recorded with a GATAN MS794 P CCD camera. The SEM and TEM experiments were conducted at the Zentrum für Elektronenmikroskopie (ZELMI) of the TU Berlin. XPS spectra were acquired on a Kratos Axis ULTRA X-ray photoelectron spectrometer. The binding energies were calibrated relative to the C 1s peak energy position as 285.0 eV. Data analyses were carried out using Casa

XPS. The surface area measurements were carried out on a Quantachrome Autosorb-1 apparatus. Nitrogen adsorption/desorption isotherms were determined at −196 °C after degassing the sample at 150 °C overnight and the BET surface areas (SBET) was estimated by adsorption data in a relative pressure range from 0.01 to 0.1.

Synthesis of $ZnCo_2O_4$, Co_3O_4, Co_3O_4@ZnO, and ZnO nanoparticles: The spinel-type and other metal oxides were synthesized by calcining at 400 °C of respective metal-carbonate hydroxide precursors, while the precursors were freshly prepared (as reported) before synthesizing the metal oxide [41]. The typical procedure for the preparation of oxide from carbonate-hydroxide is annealing the as-synthesized mixed cobalt-zinc, zinc, and cobalt hydroxide carbonate precursors at 400 °C at a rate of 2 °C/min in dry synthetic air (20% O_2, 80% N_2) in silica crucibles. A constant temperature was maintained for an additional 8 h in a tubular furnace and then cooled to room temperature to form $ZnCo_2O_4$, Co_3O_4, Co_3O_4@ZnO, and ZnO.

Chemical oxidation of water: Oxidant-driven oxygen evolution experiments were performed using aqueous solutions containing CAN as the sacrificial one electron acceptor. The oxygen evolution was measured using a Clark-type oxygen electrode system (Strathkelvin, 1302 oxygen electrode, and 782 oxygen meters). The electrode was calibrated in an air-saturated water solution and zero oxygen (sodium sulfite in water) solution prior to the experiments. In a typical reaction, 1 mg catalyst was placed in the reactor (4 mLL), which was then degassed by purging nitrogen for about 30 min. Anaerobic solution (2 mL) of 0.5 M CAN (pH 1) was then injected into the reactor to initiate the water oxidation reaction, and the oxygen evolution was monitored by a Clark electrode system under constant stirring. For all catalysts, the maximum rate of oxygen evolution was calculated using the total amount of oxygen yield after the first 60 s of reaction and represented in [$mmol_{O2}\ mol_{Co}^{-1}\ s^{-1}$].

Post-catalytic characterization: The catalysts have successfully been isolated (almost quantitatively) by precipitating out from the reaction mixture after the chemical water oxidation reaction (after 10 min). Centrifugation (at rpm of 9,000) of the reaction mixtures results in separation of heterogeneous nanoparticle catalysts, leaving the unreacted CAN and/or other inorganic ions as soluble in the aqueous phase. The resultant precipitate of the catalyst was further washed with fresh water to remove the traces of inorganic impurities. The solid mass was also dried and overnight at 60 °C and analyzed by microscopic, spectroscopic, and analytical techniques.

Declaration of competing interest

The authors declare no conflict of interest.

Acknowledgments

Funded by the Deutsche Forschungsgemeinschaft (DFG, German Research Foundation) under Germany's Excellence Strategy – EXC 2008/1 – 390540038. Gefördert durch die Deutsche Forschungsgemeinschaft (DFG) im Rahmen der Exzellenzstrategie des Bundes und der Länder – EXC 2008/1 – 390540038.

Appendix A. Supplementary data

Supplementary data to this article can be found online at https://doi.org/10.1016/j.mtchem.2019.100226.

References

[1] H.B. Gray, Powering the planet with solar fuel, Nat. Chem. 1 (2009) 7.
[2] T.A. Faunce, W. Lubitz, A.W. Rutherford, D. MacFarlane, G.F. Moore, P. Yang, D.G. Nocera, T.A. Moore, D.H. Gregory, S. Fukuzumi, K.B. Yoon, F.A. Armstrong, M.R. Wasielewski, S. Styring, Energy and environment policy case for a global project on artificial photosynthesis, Energy Environ. Sci. 6 (2013) 695.
[3] J. Li, R. Güttinger, R. Moré, F. Song, W. Wan, G.R. Patzke, Frontiers of water oxidation: the quest for true catalysts, Chem. Soc. Rev. 46 (2017) 6124–6147.
[4] M.S. Dresselhaus, I.L. Thomas, Alternative energy technologies, Nature 414 (2001) 332–337.
[5] J.J. Concepcion, R.L. House, J.M. Papanikolas, T.J. Meyer, Chemical approaches to artificial photosynthesis, Proc. Natl. Acad. Sci. U.S.A. 109 (2012) 15560–15564.
[6] I. Roger, M.A. Shipman, M.D. Symes, Earth-abundant catalysts for electrochemical and photoelectrochemical water splitting, Nat. Rev. Chem. 1 (2017) 928.
[7] B. Chakraborty, G. Gan-Or, Y. Duan, M. Raula, I.A. Weinstock, Visible-light-driven water oxidation with a polyoxometalate-complexed hematite core of 275 iron atoms, Angew. Chem. Int. Ed. 58 (2019) 6584–6589.
[8] B. Chakraborty, G. Gan-Or, M. Raula, E. Gadot, I.A. Weinstock, Design of an inherently-stable water oxidation catalyst, Nat. Commun. 9 (2018) 4896.
[9] B.M. Hunter, H.B. Gray, A.M. Müller, Earth-abundant heterogeneous water oxidation catalysts, Chem. Rev. 116 (2016) 14120–14136.
[10] T. Reier, M. Oezaslan, P. Strasser, Electrocatalytic oxygen evolution reaction (OER) on Ru, Ir, and Pt catalysts: a comparative study of nanoparticles and bulk materials, ACS Catal. 2 (2012) 1765–1772.
[11] S. Anantharaj, S.R. Ede, K. Sakthikumar, K. Karthick, S. Mishra, S. Kundu, Recent trends and perspectives in electrochemical water splitting with an emphasis on sulfide, selenide, and phosphide catalysts of Fe, Co, and Ni: a review, ACS Catal. 6 (2016) 8069–8097.
[12] C. Panda, P.W. Menezes, M. Driess, Nano-sized inorganic energy-materials by the low-temperature molecular precursor approach, Angew. Chem. Int. Ed. 57 (2018) 11130–11139. Angew. Chem. 130, (2018) 11298-11308.
[13] B. You, Y. Sun, Innovative strategies for electrocatalytic water splitting, Acc. Chem. Res. 51 (2018) 1571–1580.
[14] M.W. Kanan, D.G. Nocera, In situ formation of an oxygen-evolving catalyst in neutral water containing phosphate and Co^{2+}, Science 321 (2008) 1072–1075.
[15] P.W. Menezes, A. Indra, D. González-Flores, N.R. Sahraie, I. Zaharieva, M. Schwarze, P. Strasser, H. Dau, M. Driess, High-performance oxygen redox catalysis with multifunctional cobalt oxide nanochains: morphology-dependent activity, ACS Catal. 5 (2015) 2017–2027.
[16] P.W. Menezes, A. Indra, I. Zaharieva, C. Walter, S. Loos, S. Hoffmann, R. Schlögl, H. Dau, M. Driess, Helical cobalt borophosphates to master durable overall water-splitting, Energy Environ. Sci. 12 (2019) 988–999.
[17] P.W. Menezes, C. Panda, C. Walter, M. Schwarze, M. Driess, A cobalt-based amorphous bifunctional electrocatalysts for water-splitting evolved from a single-source lazulite cobalt phosphate, Adv. Funct. Mater. 29 (2019) 1808632.
[18] P.W. Menezes, C. Panda, S. Garai, C. Walter, A. Guiet, M. Driess, Structurally ordered intermetallic cobalt stannide nanocrystals for high-performance electrocatalytic overall water-splitting, Angew. Chem. Int. Ed. 57 (2018) 15237–15242.
[19] J. Pfrommer, M. Lublow, A. Azarpira, C. Göbel, M. Lücke, A. Steigert, M. Pogrzeba, P.W. Menezes, A. Fischer, T. Schedel-Niedrig, M. Driess, A molecular approach to self-supported cobalt-substituted ZnO materials as remarkably stable electrocatalysts for water oxidation, Angew. Chem. Int. Ed. 53 (2014) 5183–5187.
[20] R. Beltrán-Suito, P.W. Menezes, M. Driess, Amorphous outperforms crystalline nanomaterials: surface modifications of molecularly derived CoP electro(pre) catalysts for efficient water-splitting, J. Mater. Chem. 7 (2019) 15749–15756.
[21] P.W. Menezes, C. Walter, J.N. Hausmann, R. Beltran-Suito, C. Schlesiger, S. Praetz, V.Y. Verchenko, A. Shevelkov, M. Driess, Boosting water oxidation through in-situ electroconversion of manganese gallide: an intermetallic precursor approach, Angew. Chem. Int. Ed. 58 (2019) 16569–16574. Angew. Chem. 131, (2019) 16722-16727.
[22] X. Long, Z. Wang, S. Xiao, Y. An, S. Yang, Transition metal based layered double hydroxides tailored for energy conversion and storage, Mater. Today 19 (2016) 213–226.
[23] C. Panda, P.W. Menezes, S. Yao, J. Schmidt, C. Walter, J.N. Hausmann, M. Driess, Boosting electrocatalytic hydrogen evolution activity with a $NiPt_3$@NiS heteronanostructure evolved from a molecular nickel-platinum precursor, J. Am. Chem. Soc. 141 (2019) 13306–13310.
[24] P.W. Menezes, A. Indra, P. Littlewood, M. Schwarze, C. Göbel, R. Schomäcker, M. Driess, Nanostructured manganese oxides as highly active water oxidation catalysts: a boost from manganese precursor chemistry, ChemSusChem 7 (2014) 2202–2211.
[25] F. Yu, L. Yu, I.K. Mishra, Y. Yu, Z.F. Ren, H.Q. Zhou, Recent developments in earth-abundant and non-noble electrocatalysts for water electrolysis, Mater. Today. Phys. 7 (2018) 121–138.
[26] A. Indra, P.W. Menezes, M. Driess, Uncovering structure-activity relationships in manganese-oxide-based heterogeneous catalysts for efficient water oxidation, ChemSusChem 8 (2015) 776–785.
[27] P.W. Menezes, A. Indra, C. Das, C. Walter, C. Göbel, V. Gutkin, D. Schmeiβer, M. Driess, Uncovering the nature of active species of nickel phosphide catalysts in high-performance electrochemical overall water splitting, ACS Catal. 7 (2017) 103–109.
[28] A. Indra, P.W. Menezes, I. Zaharieva, E. Baktash, J. Pfrommer, M. Schwarze, H. Dau, M. Driess, Active mixed-valent MnO(x) water oxidation catalysts

through partial oxidation (corrosion) of nanostructured MnO particles, Angew. Chem. Int. Ed. 52 (2013) 13206–13210.
[29] P.W. Menezes, C. Panda, S. Loos, F. Bunschei-Bruns, C. Walter, M. Schwarze, X. Deng, H. Dau, M. Driess, A structurally versatile nickel phosphite acting as a robust bifunctional electrocatalyst for overall water splitting, Energy Environ. Sci. 11 (2018) 1287–1298.
[30] A. Indra, P.W. Menezes, M. Schwarze, M. Driess, Visible light driven non-sacrificial water oxidation and dye degradation with silver phosphates: multi-faceted morphology matters, New J. Chem. 38 (2014) 1942–1945.
[31] C. Walter, P.W. Menezes, S. Orthmann, J. Schuch, P. Connor, B. Kaiser, M. Lerch, M. Driess, A molecular approach to manganese nitride acting as a high performance electrocatalyst in the oxygen evolution reaction, Angew. Chem. Int. Ed. 57 (2018) 698–702.
[32] Q. Zhao, Z. Yan, C. Chen, J. Chen, Spinels: controlled preparation, oxygen reduction/evolution reaction application, and beyond, Chem. Rev. 117 (2017) 10121–10211.
[33] F. Jiao, H. Frei, Nanostructured cobalt oxide clusters in mesoporous silica as efficient oxygen-evolving catalysts, Angew. Chem. Int. Ed. 48 (2009) 1841–1844.
[34] Y. Liang, Y. Li, H. Wang, J. Zhou, J. Wang, T. Regier, H. Dai, Co_3O_4 nanocrystals on graphene as a synergistic catalyst for oxygen reduction reaction, Nat. Mater. 10 (2011) 780–786.
[35] X. Xie, Y. Li, Z.-Q. Liu, M. Haruta, W. Shen, Low-temperature oxidation of CO catalysed by Co_3O_4 nanorods, Nature 458 (2009) 746–749.
[36] Y. Li, W. Shen, Morphology-dependent nanocatalysts: rod-shaped oxides, Chem. Soc. Rev. 43 (2014) 1543–1574.
[37] S. Du, Z. Ren, Y. Qu, J. Wu, W. Xi, J. Zhu, H. Fu, Co_3O_4 nanosheets as a high-performance catalyst for oxygen evolution proceeding via a double two-electron process, Chem. Commun. 52 (2016) 6705–6708.
[38] W.L. Roth, The magnetic structure of Co_3O_4, J. Phys. Chem. Solids 25 (1964) 1–10.
[39] J. Xiao, Q. Kuang, S. Yang, F. Xiao, S. Wang, L. Guo, Surface structure dependent electrocatalytic activity of Co_3O_4 anchored on graphene sheets toward oxygen reduction reaction, Sci. Rep. 3 (2013) 2300.
[40] K. Krezhov, P. Konstantinov, On the cationic distribution in zinc-cobalt oxide spinels, J. Phys. Condens. Matter 5 (1993) 9287–9294.
[41] P.W. Menezes, A. Indra, A. Bergmann, P. Chernev, C. Walter, H. Dau, P. Strasser, M. Driess, Uncovering the prominent role of metal ions in octahedral versus tetrahedral sites of cobalt–zinc oxide catalysts for efficient oxidation of water, J. Mater. Chem. 4 (2016) 10014–10022.
[42] P.W. Menezes, A. Indra, V. Gutkin, M. Driess, Boosting electrochemical water oxidation through replacement of O_h Co sites in cobalt oxide spinel with manganese, Chem. Commun. 53 (2017) 8018–8021.
[43] P.W. Menezes, A. Indra, N.R. Sahraie, A. Bergmann, P. Strasser, M. Driess, Cobalt-manganese-based spinels as multifunctional materials that unify catalytic water oxidation and oxygen reduction reactions, ChemSusChem 8 (2015) 164–171.
[44] S. Sun, Y. Sun, Y. Zhou, S. Xi, X. Ren, B. Huang, H. Liao, L.P. Wang, Y. Du, Z.J. Xu, Shifting oxygen charge towards octahedral metal: a way to promote water oxidation on cobalt spinel oxides, Angew. Chem. Int. Ed. 58 (2019) 6042–6047.
[45] L. Xu, Q. Jiang, Z. Xiao, X. Li, J. Huo, S. Wang, L. Dai, Plasma-engraved Co_3O_4 nanosheets with oxygen vacancies and high surface area for the oxygen evolution reaction, Angew. Chem. Int. Ed. 55 (2016) 5277–5281.
[46] D. Zhou, L. He, R. Zhang, S. Hao, X. Hou, Z. Liu, G. Du, A.M. Asiri, C. Zheng, X. Sun, Co_3O_4 nanowire arrays toward superior water oxidation electrocatalysis in alkaline media by surface amorphization, Chem. Eur J. 23 (2017) 15601–15606.
[47] H.-Y. Wang, S.-F. Hung, H.-Y. Chen, T.-S. Chan, H.M. Chen, B. Liu, In operando identification of geometrical-site-dependent water oxidation activity of spinel Co_3O_4, J. Am. Chem. Soc. 138 (2016) 36–39.
[48] Y. Duan, S. Sun, Y. Sun, S. Xi, X. Chi, Q. Zhang, X. Ren, J. Wang, S.J.H. Ong, Y. Du, L. Gu, A. Grimaud, Z.J. Xu, Mastering surface reconstruction of metastable spinel oxides for better water oxidation, Adv. Mater. 31 (2019), e1807898.
[49] A. Indra, P.W. Menezes, N.R. Sahraie, A. Bergmann, C. Das, M. Tallarida, D. Schmeißer, P. Strasser, M. Driess, Unification of catalytic water oxidation and oxygen reduction reactions: amorphous beat crystalline cobalt iron oxides, J. Am. Chem. Soc. 136 (2014) 17530–17536.
[50] M. Yang, W. Lu, R. Jin, X.-C. Liu, S. Song, Y. Xing, Superior oxygen evolution reaction performance of $Co_3O_4/NiCo_2O_4$/Ni foam composite with hierarchical structure, ACS Sustain. Chem. Eng. 7 (2019) 12214–12221.
[51] J.B. Goodenough, A.L. Loeb, Theory of ionic ordering, crystal distortion, and magnetic exchange due to covalent forces in spinels, Phys. Rev. 98 (1955) 391–408.
[52] S.C. Abrahams, J.L. Bernstein, Remeasurement of the structure of hexagonal ZnO, Acta Crystallogr. B 25 (1969) 1233–1236.
[53] R. Matheu, P. Garrido-Barros, M. Gil-Sepulcre, M.Z. Ertem, X. Sala, C. Gimbert-Suriñach, A. Llobet, The development of molecular water oxidation catalysts, Nat. Rev. Chem. 3 (2019) 331–341.
[54] S.W. Gersten, G.J. Samuels, T.J. Meyer, Catalytic oxidation of water by an oxo-bridged ruthenium dimer, J. Am. Chem. Soc. 104 (1982) 4029–4030.
[55] Z. Codolà, I. Gamba, F. Acuña-Parés, C. Casadevall, M. Clémancey, J.-M. Latour, J.M. Luis, J. Lloret-Fillol, M. Costas, Design of iron coordination complexes as highly active homogenous water oxidation catalysts by deuteration of oxidation-sensitive sites, J. Am. Chem. Soc. 141 (2019) 323–333.
[56] F. Rong, J. Zhao, P. Su, Y. Yao, M. Li, Q. Yang, C. Li, Zinc–cobalt oxides as efficient water oxidation catalysts: the promotion effect of ZnO, J. Mater. Chem. 3 (2015) 4010–4017.
[57] M.M. Najafpour, D.J. Sedigh, B. Pashaei, S. Nayeri, Water oxidation by nano-layered manganese oxides in the presence of cerium(iv) ammonium nitrate: important factors and a proposed self-repair mechanism, New J. Chem. 37 (2013) 2448.
[58] M.M. Najafpour, B. Pashaei, Nanoscale manganese oxide within Faujasite zeolite as an efficient and biomimetic water oxidizing catalyst, Dalton Trans. 41 (2012) 10156–10160.
[59] A. Indra, P.W. Menezes, F. Schuster, M. Driess, Significant role of Mn(III) sites in e_g^1 configuration in manganese oxide catalysts for efficient artificial water oxidation, J. Photochem. Photobiol. B Biol. 152 (2015) 156–161.
[60] Y. Liang, H. Wang, J. Zhou, Y. Li, J. Wang, T. Regier, H. Dai, Covalent hybrid of spinel manganese-cobalt oxide and graphene as advanced oxygen reduction electrocatalysts, J. Am. Chem. Soc. 134 (2012) 3517–3523.
[61] U. Maitra, B.S. Naidu, A. Govindaraj, C.N.R. Rao, Importance of trivalency and the e_g^1 configuration in the photocatalytic oxidation of water by Mn and Co oxides, Proc. Natl. Acad. Sci. 110 (2013) 11704–11707.
[62] E. Ríos, H. Reyes, J. Ortiz, J.L. Gautier, Double channel electrode flow cell application to the study of HO_2- production on $Mn_xCo_{3-x}O_4$ ($0 \leq x \leq 1$) spinel films, Electrochim. Acta 50 (2005) 2705–2711.
[63] Y. Li, P. Hasin, Y. Wu, $Ni_{(x)}Co_{(3-x)}O_{(4)}$ nanowire arrays for electrocatalytic oxygen evolution, Adv. Mater. 22 (2010) 1926–1929.
[64] B.S. Yeo, A.T. Bell, Enhanced activity of gold-supported cobalt oxide for the electrochemical evolution of oxygen, J. Am. Chem. Soc. 133 (2011) 5587–5593.
[65] J.G. McAlpin, Y. Surendranath, M. Dinca, T.A. Stich, S.A. Stoian, W.H. Casey, D.G. Nocera, R.D. Britt, EPR evidence for Co(IV) species produced during water oxidation at neutral pH, J. Am. Chem. Soc. 132 (2010) 6882–6883.